4DPrinted MagnetoPlasmonic Microrobots for Programmable Spatiotemporal DeIcing

Advanced Functional Materials

ADVANCED FUNCTIONAL MATERIALS
www.afm-journal.de

RESEARCH ARTICLE OPEN ACCESS

4D-Printed Magneto-Plasmonic Microrobots for Programmable Spatiotemporal De-Icing

Amélie Pérot[1] | Andrea Cosola[2,3] | Eléonore Aïdonidis[2] | Jérôme Fresnais[4] | Clément Sanchez[1,5] | Philippe Belleville[6] | Giancarlo Rizza[2] | Marco Faustini[1,7]

[1]CNRS, UMR 7574 Chimie de la Matière Condensée de Paris, Sorbonne Université, Paris, France | [2]Laboratoire des Solides Irradies (LSI), CEA/DRF/IRAMIS, Ecole Polytechnique Institut Polytechnique de Paris, Palaiseau, France | [3]Department of Applied Science and Technology, Politecnico di Torino, Torino, Italy | [4]CNRS, Laboratoire de Physico-chimie des Electrolytes et Nanosystèmes Interfaciaux, PHENIX—UMR 8234, Sorbonne Université, Paris, France | [5]University of Strasbourg Institute for Advanced Study (USIAS), Strasbourg, France | [6]CEA, DAM, Le Ripault, Monts, France | [7]Institut Universitaire de France, Paris, France

Correspondence: Giancarlo Rizza (giancarlo.rizza@polytechnique.edu) | Marco Faustini (marco.faustini@sorbonne-universite.fr)

Received: 13 November 2025 | **Revised:** 17 February 2026 | **Accepted:** 27 February 2026

Keywords: 4D printing | digital light processing | icing | magnetic actuation | photothermal | plasmonics

ABSTRACT

Icing poses a significant challenge in energy, transportation, and (soft) robotic applications, leading to disfunctions and efficiency losses. Traditional de-icing methods are often energy-intensive, non-selective, or difficult to integrate with robotic and autonomous systems. Here, we introduce a 4D-printing strategy that enables programmable spatio-temporal de-icing, providing an energy-efficient pathway to precisely control when and where ice is removed at the millimeter scale. By integrating raspberry-like gold–magnetite nanofillers into a photosensitive resin and employing a magnetic-assisted Digital Light Processing (DLP), we align the fillers into oriented nanoparticle chains, producing anisotropic architectures with dual functionality: magnetic-driven mobility actuation and plasmonic heating for localized thermal release. Hyperspectral analysis shows that the photothermal response can be finely tuned through plasmonic grafting density, while geometric programming governs the amplitude and spatial distribution of heating. As a demonstration of this multifunctional platform, we develop an autonomous icebreaking microrobot capable of navigating frozen landscapes while melting ice with pinpoint accuracy. This work introduces a new class of 4D-printed magneto-plasmonic materials enabling on-demand phase-transition control, opening opportunities for energy-efficient de-icing, adaptive soft robotics for extreme environments and time-programmable devices.

1 | Introduction

In the last decades, additive manufacturing has grown up as an essential technique for material design [1, 2]. Based on its technological advances, 4D printing has emerged in 2013 [3]. Initially defined as the 3D printing of objects capable of changing shape in response to a stimulus, the definition has since broadened. Today, 4D printing encompasses the 3D fabrication of objects that can change at least one of their properties or functionalities over time under external stimuli [4, 5]. While the most spread example consists in using temperature as a stimulus to modify the shape of the object [6–9], several other stimuli, such as light [10, 11], magnetic field [12, 13], electric field [14], solvent [15, 16], pH [17] have been also explored in the literature to induce different responses, including shift in color [18], remote locomotion [19, 20] and actuation [21–23]. Owing to their ability to integrate responsiveness directly into 3D-printed structures, 4D-printed devices have been proposed for applications across a wide range of domains. Yet, most current architectures still operate in a single-stimulus, single-response regime, highlighting the untapped potential for richer, coupled functionalities. Among these, photothermal actuation remains scarcely explored

with only a few examples, such as plasmonic heating-mediated shape recovery in protein nanocomposites [24]. As a result, photoheating offers a largely untapped route for remote and selective thermal control, enabling new modes of functional, light-programmable behavior. Beyond the context of additive manufacturing, the photothermal effect is already well established in other fields. In biomedicine, for example, near-infrared-responsive absorbers are employed for targeted photothermal therapy to destroy cancer cells or to enable controlled drug release [24]. In microfluidics, light-induced temperature changes can precisely manipulate flow patterns and chemical reactions [25]. Important for everyday-life applications, photoheating can induce phase transitions, for instance, in antifogging coatings: the localized heating prevents water droplet condensation and accelerates evaporation on optical lenses or windshields [26]. Light-driven water evaporation has also been used to develop water purification systems [27], homeostatic coatings [28, 29], or even to manipulate crack propagation [30]. In this broader context, icing remains a critical challenge for renewable energy, aviation, marine operations, and sensitive electronics, leading to significant energy losses and compromised performance [31]. Among de-icing strategies, photothermal coatings have shown promise, using light as a remote and controllable trigger [32, 33]. Thus, extending photothermal de-icing to 4D devices could open new avenues for autonomous ice management, particularly in (soft)robotics enabling small robotic platforms or drones to navigate icy environments, actively sculpt or remove ice, and respond dynamically to freezing conditions. Localized heating, combined with locomotion or shape-morphing capabilities, would allow these systems to concentrate energy only where needed, improving efficiency and adaptability in severe environments. Despite this potential, photothermal de-icing has not yet been demonstrated in 4D-printed systems.

To address this challenge, we introduce a 4D-printing strategy that employs magneto-plasmonic photoheaters to achieve spatio-temporal de-icing, providing precise control over both location and rate of ice melting. To achieve the desired properties, our approach combines two stimuli: magnetic fields to control the object's locomotion (spatial positioning) and light to trigger localized heating (thermo-temporal activation). Magnetic-assisted Digital Light Processing [34] (DLP) is used to fabricate active structures composed of spatially aligned chains of magneto-plasmonic nanofillers dispersed within a photosensitive resin. This configuration enables precise rotational and translational control of the printed objects while simultaneously allowing localized photothermal heating. As a proof of concept, we fabricated a 4D-printed magneto-plasmonic icebreaker ship, showcasing autonomous ice-management capabilities. This work pioneers a novel application domain for 4D printing where plasmonic nano-heaters are integrated within magneto-responsive architectures for spatiotemporal control of ice–surface interactions for active and programmable anti-icing/de-icing systems. Although purely magneto-active 4D-printed devices have been previously reported (Table S1), the development of multi-functional magneto-plasmonic 4D-printed constructs remains a significant challenge. This difficulty arises from the non-trivial integration of both magnetic and heat-emitting fillers within a single printed architecture. In addition, the high polydispersity of most commercially available magnetic fillers hinders precise optical control and limits the efficiency of photo-thermal design. Addressing these gaps demands a multidisciplinary approach that combines advances in nanomaterial synthesis, resin formulation, additive manufacturing, and functional characterization. The present approach moves beyond the mere combination of independent functionalities and demonstrates a synergistic platform in which magnetic actuation enables precise positioning and mechanical interaction, whereas plasmonic heating provides localized, rapid, and contactless thermal input. Unlike conventional resistive de-icing systems, our approach is specifically designed for untethered, mobile microrobotic platforms enabling both contactless actuation and photo-thermal heating through magnetic fields and light. More broadly, the proposed magneto-plasmonic architecture represents a first step toward the design of 4D-printed devices in applications where coordinated mechanical motion and localized energy delivery are required, such as ice management and soft robotics in harsh conditions.

2 | Results and Discussion

2.1 | Design of the Magneto-Plasmonic Photoheater

The general design of a programmable photoheater is illustrated in Figure 1. The 4D-printed object is a hierarchically structured construct, combining a macroscopic passive element with a microscopic functional architecture composed of raspberry-like magneto-plasmonic assemblies, consisting of magnetite (Fe_3O_4) cores decorated with spherical gold (Au) nanoparticles. The nanofillers are self-assembled into aligned, chain-like structures, introducing magnetic anisotropy into the printed element, while enabling tuning of their plasmonic properties through controlled interparticle interactions. In particular, the interaction between the chains and the applied magnetic field enables precise control over the object's movement. Specifically, misalignment between the chains' magnetic moments and the applied field drives chain realignment, i.e., $\tau = mxB$, resulting in rotation of the printed object along the field direction. Meanwhile, the magnetic field gradient generates a directional force on the chains, i.e., $F = \nabla(m \cdot B)$, allowing controlled translational movement of the object. Besides, upon light irradiation, the plasmonic assemblies within the magneto-plasmonic fillers generate localized heat, enabling temporal control of the heated region. As an example, Figure 1 showcases an illustration of a 4D-printed icebreaker ship that combines magnetic actuation and photothermal heating. Upon light exposure, it melts the surrounding ice, while the applied magnetic field drives it forward, allowing it to cut through ice by melting it in real time.

To fabricate these hierarchically structured devices, we use a custom magnetic-assisted DLP apparatus featuring a nested Halbach array integrated with a vertically aligned coil, which enables precise control of both the intensity and orientation of the magnetic field in 3D space, Figure 2 [35]. A Halbach array is a specific arrangement of permanent magnets that enhances the magnetic field on one side while nearly canceling it on the opposite side. Ideally, a Halbach array can be modeled as an infinitely long cylinder with continuously rotating magnetization [36]. In practice, however, this is not feasible, and real Halbach arrays are constructed using discretization methods. The cylinder is divided into P magnets (Figure 2 in red) of identical shape and

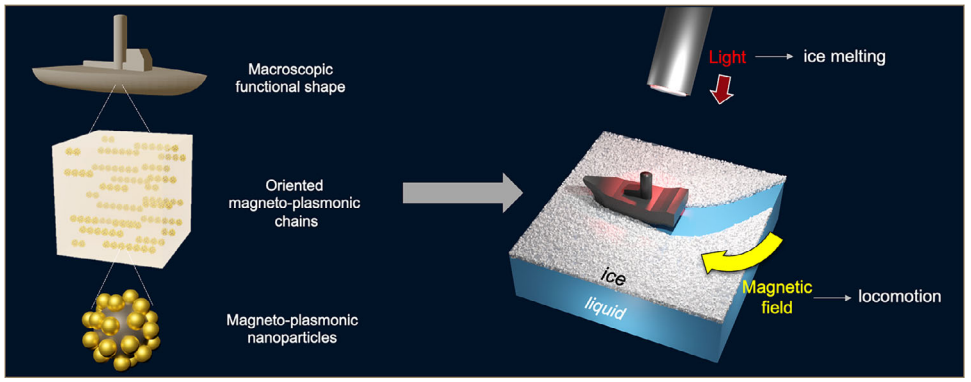

FIGURE 1 | Example of a 4D printed photoheater used as an icebreaking ship. The 4D printed device presents a macroscopic functional shape (e.g., icebreaker ship) and embedded chain-like aligned magneto-plasmonic fillers. The magnetic field drives locomotion (spatial positioning) while the light irradiation enables a heat trigger (temporal control of the melting speed).

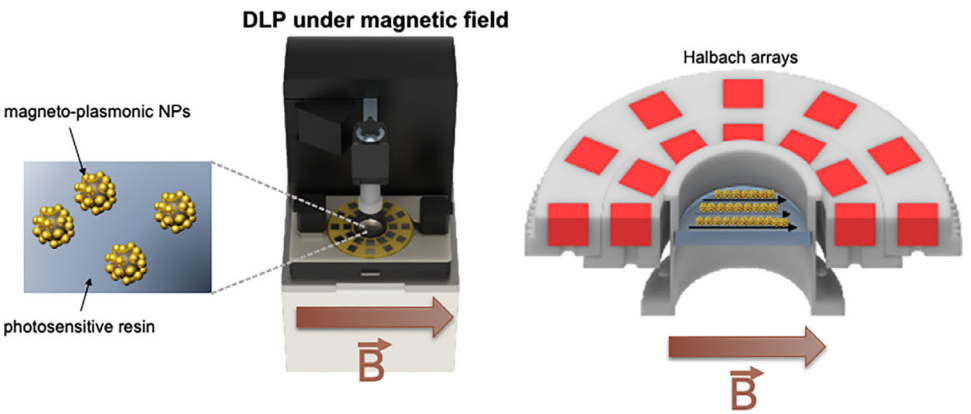

FIGURE 2 | Fabrication principle of the magneto-plasmonic photoheater. The object is printed by Digital Light Processing by using a polymeric resin loaded with the magneto-plasmonic fillers. The vat is exposed to a unidirectional magnetic field that aligns the particles in the field direction. Two Halbach arrays of magnets are used to create the field in the *xy* plane. They can rotate to modulate the final intensity of the magnetic field in the plane by vectorial construction. Set up protected by patent pending No. WO2025073835A1.

magnetization magnitude, but with different orientations, where the direction of each magnetic dipole, φ, is an integer multiple of its angular position, θ, such that $\varphi = (k+1)\theta$. The field polarity of the Halbach array is characterized by the parameter k; for example, a dipolar configuration ($k = +1$) produces a uniform magnetic field within the printing region. Thus, the vat of the DLP printer is exposed to a homogeneous oriented magnetic field enabling formation and alignment of the magneto-plasmonic chains during the fabrication process, as will be detailed later on.

2.2 | Synthesis and Self-Assembly of Magneto-Plasmonic Nanoparticles

Magneto-plasmonic magnetite-gold nanoparticles serving as *two-in-one* multifunctional filler. One challenge concerns the synthesis of these magneto-plasmonic nanofillers with controlled thermo-plasmonic properties. As mentioned before, most commercially available magnetic fillers are highly polydisperse and strongly light-scattering, which severely limits optical tunability and makes the design of efficient and predictable plasmonic heating extremely difficult. To address this bottleneck, we developed the synthesis of monodisperse magneto-plasmonic nanofillers, specifically engineered to ensure production at the gram scale (for device fabrication) while remaining compatible with photocurable resins and DLP printing. To do so, first, magnetic nanoparticles (MNP) were synthesized and subsequently functionalized with polyethyleneimine (PEI) [37]. They consist of monodisperse spherical particles with an average diameter of 75 ± 10 nm (Figure S1). In parallel, gold nanoparticles were produced using the Turkevich method [38]. They exhibit an average diameter of 18 ± 5 nm (Figure S2) and are stabilized by a citrate layer. The two types of nanoparticles were subsequently mixed in water under ultrasonic agitation to promote homogeneous dispersion. The PEI coating on the magnetic nanoparticles provides terminal amino groups and a positive surface charge, enhancing their colloidal stability and enabling the electrostatic assembly of negatively charged gold nanoparticles onto their surface [39]. The resulting composite magneto-plasmonic fillers collected by magnetic separation exhibit a raspberry-like morphology, with gold nanoparticles uniformly decorating the surface of the magnetic cores as confirmed by Transmission Electron Microscopy (TEM), Figure 3a,b. The grafting density of gold nanoparticles was optimized by adjusting both the volume of the gold nanoparticle

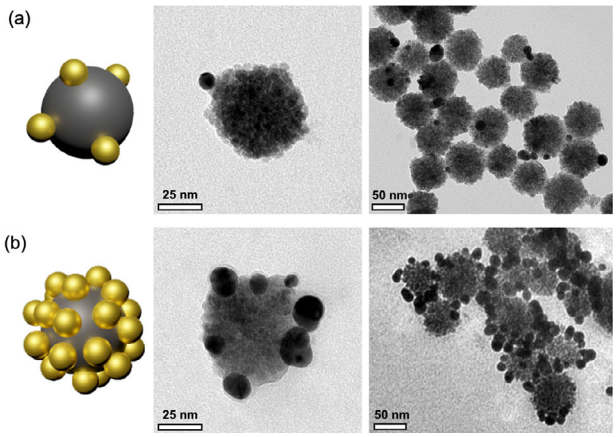

FIGURE 3 | Illustrations and TEM micrographs of the magneto-plasmonic fillers with two grafting densities: (a) MNP@Au_28 and (b) MNP@Au_3.

solution relative to the mass of magnetic nanoparticles and the concentration of the gold nanoparticle suspension. In this work, two sub-systems were investigated: the first presents a high gold grafting density (atomic Au/Fe ratio = 27.9 ± 4.9%, Figure 3a), while the second one presents a lower grafting density (atomic Au/Fe ratio = 2.7 ± 0.3%, Figure 3b). In the following, these samples are referred to by their atomic ratios as MNP@Au_28 and MNP@Au_3, respectively.

To form a printable composite formulation, magneto-plasmonic nanofillers were dispersed into a bisphenol A ethoxylate diacrylate (BEDA) resin using bis(2,4,6-trimethylbenzoyl) phenylphosphine oxide (BAPO) as photoinitiator. The viscosity of the final formulation represents a compromise between the temporal stability of the embedded filler dispersion, needed to keep the particles suspended, and the printability of the resin, which requires sufficient flow between layer depositions during the Digital Light Processing (DLP) process. As shown in Figure S3, the unloaded resin exhibits shear-thickening behavior at low shear rates (<0.07 s^{-1}) and reaches a stable viscosity plateau at higher shear rates. In this regime, the viscosity was measured at 211 ± 2 mPa·s, which lies within the typical range reported for DLP-printable resins (0.001–1 Pa.s) [40]. Furthermore, as shown in Figure S4a, the filler dispersion remains stable for at least 31 h (a time much longer than the one necessary for a typical printing session). This enables the fabrication of macroscopic objects with a uniform distribution of nanofiller as demonstrated in Figure S4b. The resin is then poured into the vat of the DLP printer and exposed to a uniform and unidirectional magnetic field to induce the self-assembly of the raspberry-like gold–magnetite into chain structures, which are subsequently frozen within the printed object through the layer-by-layer photopolymerization. The magnetic field intensity was set to 10 mT following a previous experimental procedure [35], a value enabling to both avoid migration of particles toward edges of the vat [34] and forming stable chains of aligned structures.

The duration of the applied magnetic field determines the length of the chains formed within the formulation, making the chain-formation time a critical parameter. To optimize this process, we systematically investigated the kinetics of nanoparticle assembly and alignment using optical microscopy. In particular, the resin containing the magneto-plasmonic fillers (without photoinitiator) was spread on a glass substrate and then exposed to a uniform magnetic field of 10 mT (Figure 4a). Finally, the self-assembly process was monitored in real time using a LEICA DM optical microscope. Figure 4b presents the time evolution of the assembly for a filler loading of 0.2 phB (per hundred BEDA, defined as phB = m_MNP / m_BEDA × 100) up to 30 min. Initially, small chains form, which gradually coalesce into larger, anisotropic aggregates with a polydisperse size distribution. The temporal evolution of chain length, represented by the 5th, 95th percentiles, and the average, was obtained from image analysis, Figure 4c. Under these conditions, the average chain length increased with time, reaching a plateau after approximately 30 min. Notably, anisotropic chains were already formed after 15 min, corresponding to about 75% of their final average length. Accordingly, a 15-min magnetic field application was chosen as an optimized processing condition, providing an effective balance between adequate chain formation and minimization of processing time. Finally, Figure 4d shows the final chain morphology as the filler loading is increased from 0.1 to 2.0 phB. Higher loadings generally lead to the formation of longer chains until coalescence processes dominate [41].

2.3 | Magnetic Properties of 4D Printed Devices

Room-temperature hysteresis loops were measured to evaluate the magnetic behavior of the DLP-printed nanocomposites, Figure 5a [42, 43]. For samples printed with a filler loading of 0.5 phB MNP, no major differences are observed in the hysteresis loop whether chain structures are present or not. The magnetization at saturation reaches 60 emu/g for a magnetic field H exceeding 10 kOe. For MNP@Au_28, the magnetization at saturation is slightly lower, reaching 53 emu g^{-1} for the same range of magnetic field H. The samples exhibit only a small hysteresis at low magnetic fields, with behavior approaching that of superparamagnetic materials, Figure 5b. A first indication of anisotropic response can be observed in Figure S5a; the hysteresis loops show that there is an anisotropy, or easy magnetization axis, when the chains are aligned parallel to the external field. This means that it is easier to reach saturation when the field is applied in the direction of the chains than in the perpendicular direction, as already reported in the literature for oriented chains of magnetic objects [44].

As mentioned above, the printed objects with embedded chains possess anisotropic magnetic properties that enable magnetic actuation: orientation and translation. To control the rotation of the object, the presence of oriented chains is the key. This is demonstrated by printing two hammers (loading of 1 phB), each with a different chain orientation: (Figure 5c), perpendicular (⊥) and parallel (∥) to its handle, respectively. As shown in Figure 5d, both hammers float on water and are held by the end of the handle, remaining free to rotate around the fixation point. When exposed to a uniform magnetic field (10 mT) a torque acts, i.e., $\tau =$ mxB, such that each hammer rotates to align the chains along the direction of the applied field. As reported in the Video S1, if the direction of the field is modified, the hammers adjust accordingly. As shown in Video S2 and Figure 5e, inducing translation of the oriented magneto-plasmonic composites requires applying a magnetic field gradient, such as that produced by a permanent

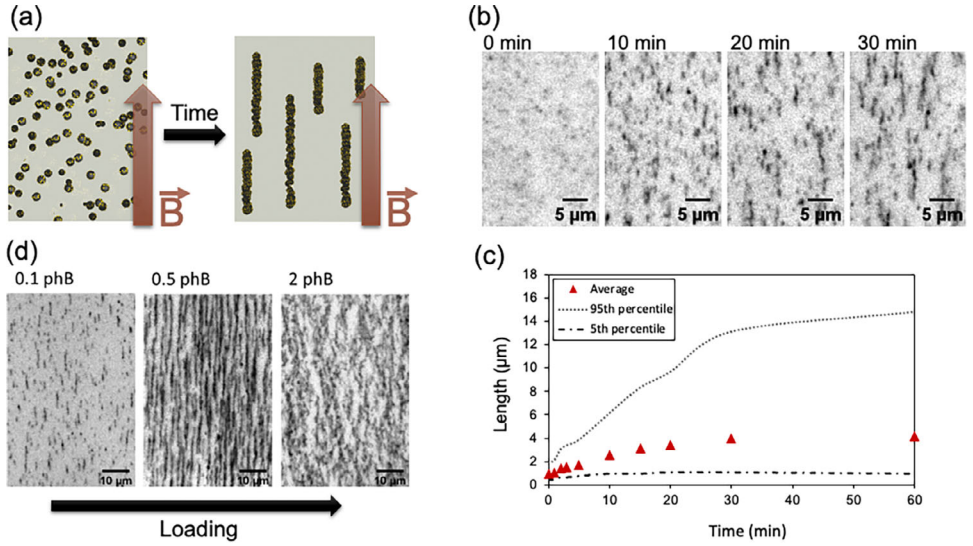

FIGURE 4 | Assembly of particles into chain-like structures (results for load with MNP@Au_28, magnetic field of 10 mT). (a) Scheme of the principle of the assembly. Particles are initially dispersed into the liquid resin. The resin is exposed to a uniform unidirectional magnetic field, the particles self-assemble into chains in the direction of the magnetic field. (b) In situ optical microscope imaging of chain's formation in a thin film during the assembly step through time, for a loading of 0.2 phB. (c) Evolution of the length of chains with time load of 0.2 phB. (d) Optical microscope images of the microstructure morphology for increasing loading with 0.1, 0.5, and 2 phB, after 20 min of exposure to the magnetic field.

magnet. In this case, the objects move toward regions of higher field strength, following, i.e., $F = \nabla(m \cdot B)$.

2.4 | Optical Properties and Photoheating Capabilities of the 4D Printed Devices

To enable the second functionality, light-induced heat generation, precise control over the optical properties of the plasmonic systems is crucial. Heat is generated only when the plasmonic resonance is excited at the appropriate wavelength, which is typically characterized by its absorbance and scattering response [45]. These properties can be tuned through coupling between plasmonic particles, which can create "hot spots" leading to more efficient light absorption and highly localized heat generation [45, 46]. As a consequence, by increasing the density and proximity of plasmonic particles to maximize coupling and hot-spot formation, the efficiency of light-to-heat conversion can be significantly enhanced [47]. To investigate the optical properties of our systems, we prepare films on glass substrates using a film applicator bar. These films are made from the polymerized resin, approximately 10 µm thick, with a charge of 0.5 phB of either MNP (without gold NPs), MNP@Au_3 (low gold NP charge), or MNP@Au_28 (high gold NP charge), with particles aligned (under 10 mT).

As illustrated in Figure 6a, samples were characterized by hyperspectral microscopy in dark-field mode. This technique enables optical imaging in which each pixel contains the local optical spectrum of the sample [48, 49]. In transmission dark-field mode, it allows for mapping the scattering intensity at the single-object level. The dark-field micrographs shown in Figure 6b display the chains for the MNP@Au_3 and MNP@Au_28. The scattering spectra shown in Figure 6c present a global scattering contribution resulting from an average on all the pixels of the image. For MNP@Au_3, the spectrum is comparable to the one of MNP (without Au). MNP@Au_28 shows a strong plasmonic scattering signal with a maximum at 609 nm. The band is broad and extends until the near infrared wavelengths. To qualitatively highlight the contribution of the Au NPs in the signal (that are main responsible for photoheating as discussed later on), the spectra of MNP@Au were normalized by the one of MNP [50]. As shown in Figure 6d, the characteristic shape of each normalized spectrum provides information about the type of plasmonic interactions. For both samples a broad intense scattering contribution is detected in the Near Infra-Red (NIR) between 800 and 1000 nm. For MNP@Au_3, some weaker bands of scattering emerge, the first one between 530 and 600 nm and the second between 650 and 710 nm. The first band is characteristic of isolated gold NP, while the second one could be attributed to the presence of a dimer of gold NPs [51]. A mapping of each contribution on the image is presented on Figure S5b. More interestingly, for MNP@Au_28, the plasmonic contribution is broader and more intense going from green to NIR-light, with the highest scattering in red and near infrared section. For MNP@Au_28, a such broad signal is characteristic of aggregates of gold nanoparticles and plasmonic coupling [52]. This plasmonic response originates from the collective optical behavior of raspberry-like magneto-plasmonic nanofillers assembled into chains under a magnetic field. Each nanofiller consists of multiple Au nanoparticles randomly distributed on the surface of a Fe_3O_4 core as shown in Figure 3b, while the magnetic assembly process leads to the formation of chains along the field direction with non-periodic interparticle distances. This hierarchical structural disorder, present both at the single-particle and chain levels, results in a wide distribution of plasmonic coupling configurations rather than a single, well-defined resonance mode. To prove that, we used hyperspectral optical microscopy to directly probe the plasmonic response of the real structures. Spatially resolved scattering spectra acquired at different locations along individual chains (Figure S6) reveal pronounced heterogeneity in the optical response, evidencing multiple locally coupled plasmonic modes. In particular, chains

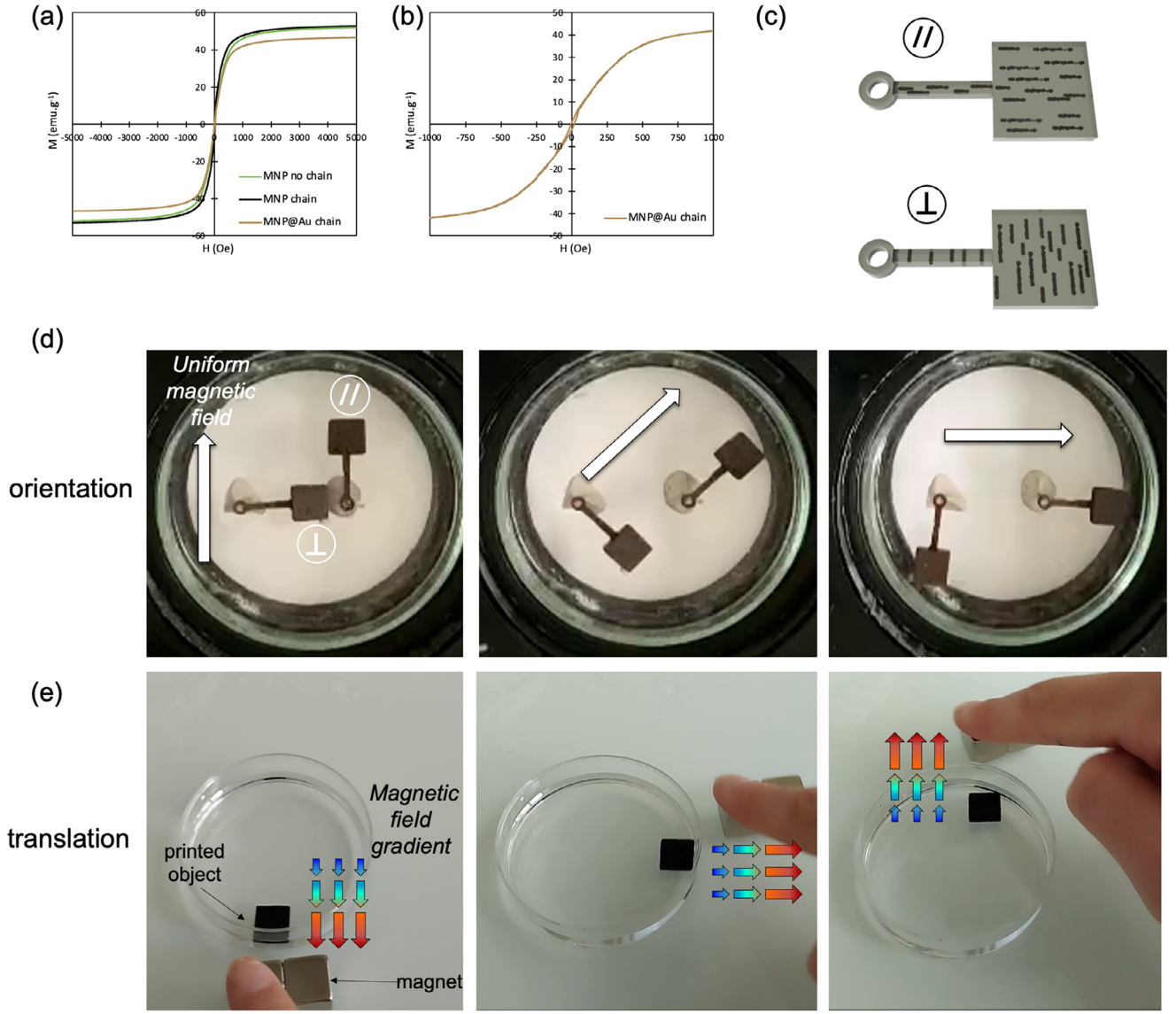

FIGURE 5 | Magnetic properties of printed systems. (a) Room temperature hysteresis loops of printed pieces with not aligned MNP, aligned MNP or aligned MNP@Au_28 with 0.5 phB. (b) Zoom into low field region of the hysteresis loop of MNP@Au_28. (c) Schematic illustration of two printed hammer-shaped samples and their corresponding internal chain orientations: the top sample features chains perpendicular to the main axis of the hammer, while the bottom sample features chains parallel to it. (d) Photographs showing the two hammers exposed to a rotating homogeneous magnetic field. Each hammer rotates to align its embedded chains with the direction of the applied magnetic field. (e) Photographs showing the translation of a magnetic printed object in the presence of a gradient of magnetic field.

composed of Au-rich nanofillers (MNP@Au_28, Figure S6a) exhibit several scattering contributions in the 600–750 nm range, appearing either as a broad resonance or as partially overlapping peaks depending on the probed location. The integration of these local responses results in the global scattering spectrum reported in Figure 6c. In contrast, isolated magneto-plasmonic nanoparticles dispersed in solution display a narrow plasmonic peak centered at approximately 545 nm, characteristic of uncoupled Au nanoparticles (Figure S7). The strong red-shift and spectral broadening observed upon chain formation therefore provide clear experimental evidence of near-field plasmonic coupling.

This behavior is fully consistent with extensive literature on disordered plasmonic assemblies, where random geometries lead to broadened, red-shifted resonances and spatially distributed electromagnetic hot spots rather than discrete, well-defined modes [45, 53, 54]. The results also indicate that depending on the density of grafting of gold nanoparticles, the optical and photo-thermal response can be, in part, modulated.

For practical applications such as de-icing, we focus on maximizing heat generation by examining the photoheating effect of the magneto-plasmonic system with the highest gold grafting density, MNP@Au_28. This system exhibits a broad plasmonic scattering contribution spanning from visible to near-infrared wavelengths NIR. In particular, we investigate the photo-thermal heating of the same MNP@Au_28 film with lasers at two wavelengths: in the visible range (532 nm) and in the NIR (852 nm). First, the impact of the light intensity was studied by measuring the increase in temperature with a FLIR E6 thermal camera, Figure 6e. In both

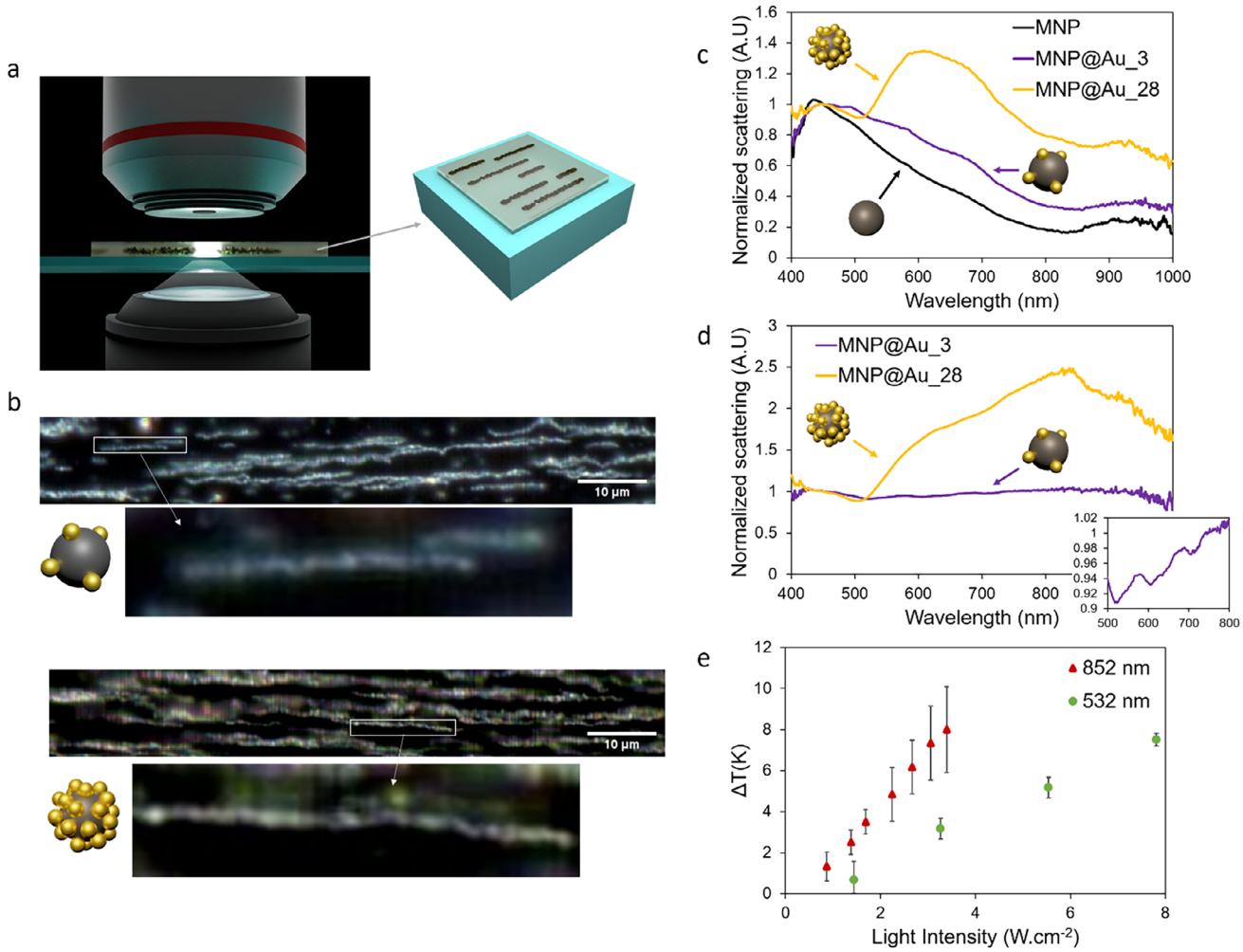

FIGURE 6 | Optical properties of the loaded films. (a) Schematic illustration of the dark-field hyperspectral microscope. (b) dark field hyperspectral micrographs of the chains made of MNP@Au_3 and MNP@Au_28. (c) Global normalized scattering spectra of thin films loaded with 0.5 phB containing different types of particles (MNP, MNP@Au_28, MNP@Au-3). (d) Scattering spectra of MNP@Au_3 and MNP@Au_28 thin film normalized with MNP contribution. Inclusion is a zoom into the spectra of @Au_3. (e) Photothermal heating for the MNP@Au_28 film: increase of temperature as function of the light intensity at two different wavelengths.

cases, temperature rises linearly with light intensity, yet heating is notably more efficient at 852 nm than at 532 nm, exhibiting slopes of 2.7 and 1.0 $K{\cdot}cm^2{\cdot}W^{-1}$, respectively. These results are in agreement with those shown Figure 6d, indicating a larger plasmonic scattering signal in the NIR. To investigate the photothermal capabilities of macroscopic objects, we first print 1 cm^2 squares, 0.2 mm thick sample using resin loaded with 0.5 phB of MNP (without gold) and MNP@Au_28, with particle alignment achieved under a 10 mT magnetic field, Figure 7a. Samples were exposed to both lasers (532 and 852 nm) at a light intensity of 0.60 Wcm^{-2}. Figure 7b shows that photoheating is greater for MNP@Au_28, highlighting the contribution of the plasmonic absorbers, as plasmonic heating is more efficient than the photothermal effect of MNP alone. For MNP, heating at 532 nm is greater than at 852 nm, consistent with the higher absorption of MNP at 532 nm compared to 852 nm, Figure S8. In contrast, for the plasmonic sample MNP@Au_28, irradiation at 852 nm raises the temperature above 80°C, significantly higher than with the green laser (532 nm), in agreement with the results on glass-supported films shown in Figure 6e. At 852 nm, the plasmonic resonance is effectively excited, triggering the collective mode of resonance of aggregates on the surface of the MNP. The photothermal conversion efficiency of the MNP@Au_28 was quantified using an energy-balance method adapted from the procedure originally introduced by Roper et al. [55] for plasmonic photothermal materials ("Photothermal conversion efficiency analysis" section in Supporting Information). This approach relates the steady-state temperature rise of an illuminated object to the absorbed optical power and the heat dissipated to the surroundings via conduction, convection, and radiation. Thus, sample exhibits a photothermal conversion efficiency of approximately 40% under 852 nm laser irradiation.

We then examined how sample thickness affects the photothermal response of the printed composites, as shown in Figure 7b. To this end, square samples (1 cm^2) with thicknesses ranging from 0.2 to 2 mm were printed, and their temperature increases under illumination were measured. Unlike the experiment shown in Figure 6e, the composite samples were not supported on glass. Each sample was exposed to both lasers at a light intensity

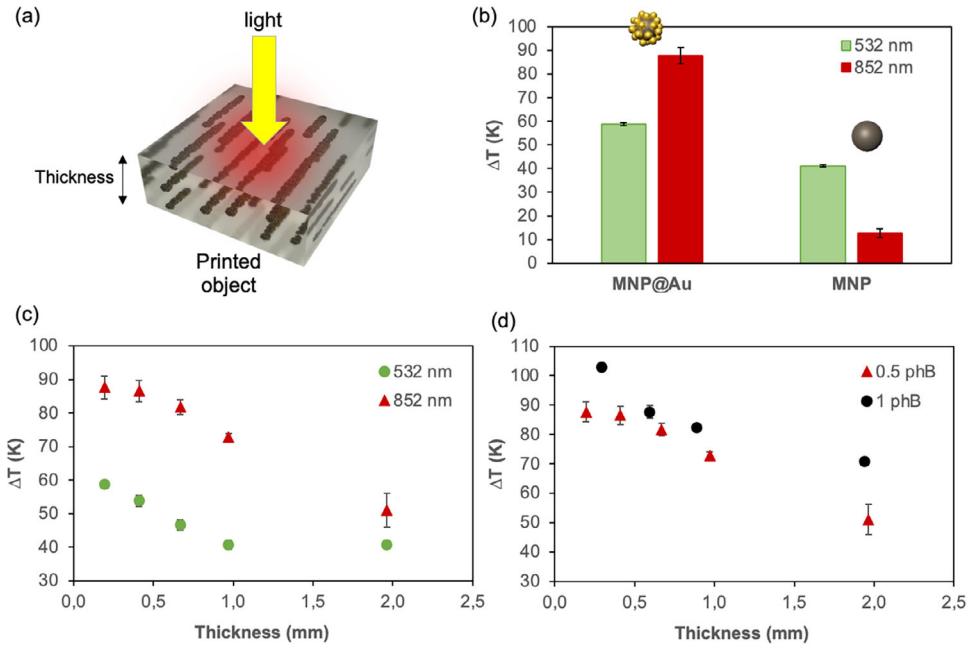

FIGURE 7 | (a) Measurements of the photoheating properties of printed pieces. (b) Increase of temperature of a 0.2 mm thick printed piece loaded with 0.5 phB of MNP@Au_28 or 0.5 phB of MNP under 532 nm and 852 nm at light intensity of 0.60 W cm^{-2}. The contribution of gold NPs to the heating is more significant at 852 nm than at 532 nm, with a global higher heating at 852 nm than at 532 nm. (c) Increase of temperature in RT conditions depending of the thickness of the printed piece, loaded with 0.5 phB of MNP@Au_28, under 532 and 852 nm at light intensity of 0.60 W cm^{-2}. (d) Increase of temperature depending of the thickness of the printed piece, loaded with 0.5 and 1 phB of MNP@Au_28, under laser at 852 nm at light intensity of 0.60 W cm^{-2}.

of 0.60 W cm^{-2}. Within this range, the heating efficiency decreased as the thickness increased. This behavior indicates that plasmonic heating is governed by surface-dominated absorption, meaning that the light-absorbing region is thinner than the minimum tested thickness (0.2 mm). The generated heat near the surface is then dissipated into the cooler surrounding material; thus, thicker samples spread the heat over a larger volume, leading to a lower measured temperature increase. Additional analysis (reported in the "Photothermal conversion efficiency analysis" section in Supporting Information) indicated that the estimated optical penetration depth is around 61 μm at 852 nm.

Finally, we examined the effect of MNP@Au loading (0.5 and 1 phB) under 852 nm illumination. Increasing the loading slightly enhances photothermal heating, but the temperature rise remains limited even when the nanoparticle concentration is doubled. This is attributed to the increased optical opacity of the composite at higher loadings: as more particles are incorporated, the effective optical penetration depth decreases, confining light absorption to a thinner surface layer. Consequently, nanoparticles embedded deeper in the material receive less light and contribute minimally to heating. Thus, the overall improvement in photothermal efficiency is not proportional to the particle concentration, consistent with a surface-dominated absorption mechanism. In summary, while the filler loading used for printing has only a limited influence on the object's heating performance, the thickness of the printed part plays a more crucial role. More broadly, the light intensity and wavelength of the illumination source represent the most effective parameters for achieving and tuning localized photothermal heating, particularly for de-icing applications.

2.5 | Proof of Concept of a Magneto-Plasmonic De-Icing Device

Based on previous magnetic and optical investigations, a magneto-plasmonic icebreaker ship was printed as a proof of concept for spatio-temporal controlled de-icing (Figure 8a). We first demonstrate the ship's capability to heat and melt ice using NIR light. To achieve this, a Peltier module was used to create a thin, thermo-regulated layer of ice at around −5°C. As shown in Figure 8b, we first measure the temperature increase with a thermal camera. Without the printed ship, the glass support exposed to NIR light for 5 min showed no temperature increase, while with the ship in place, the temperature rose above 55°C. Figure 8c shows the same experiment on a layer of ice. Prolonged irradiation with NIR light alone did not modify the ice layer. In contrast, the printed ship melted the underlying ice in less than 2 min (Video S3).

Finally, we demonstrate the dual functionality of our printed device (see Figure S9 for more details on the design). In this case, the loading was 1% phB of MNP@Au NPs to ensure a sufficient magnetic response to the applied magnetic field while maintaining efficient photoheating. Two printed icebreaker ships are initially placed on a thin layer of ice, resting on cold liquid water, similar to sea ice conditions (Figure 9a). A magnet is positioned next to the water container while a light source at

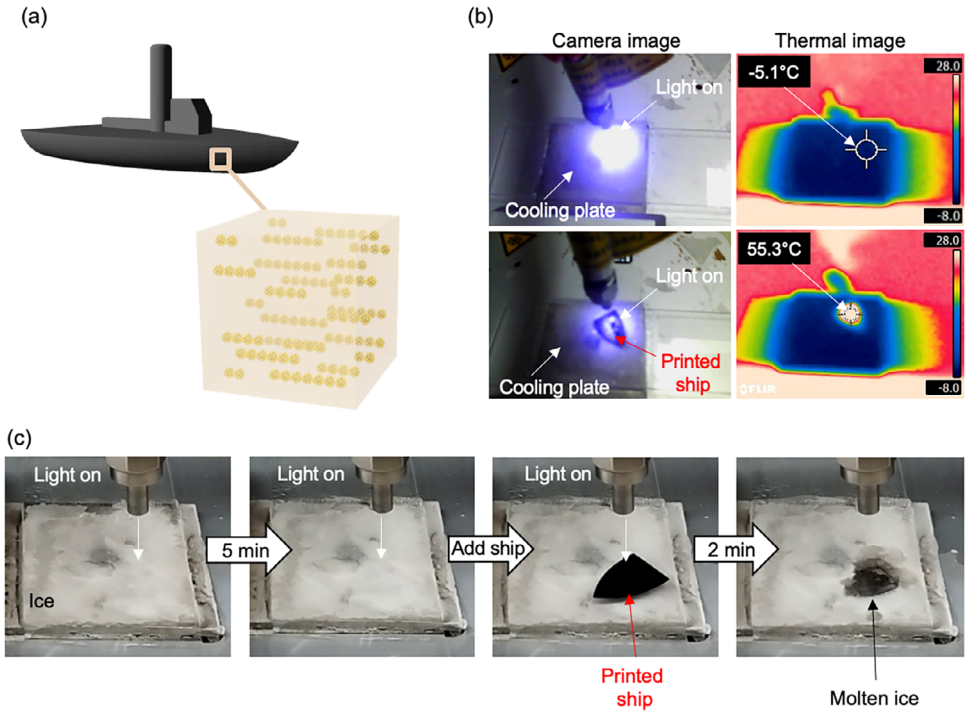

FIGURE 8 | (a) Scheme of the magneto-plasmonic icebreaker ship. (b) Heating capability of the ship. Control experiment by IR camera: no temperature raise is observed after 5 min of irradiation with nIR light (top) while the photoheater ship heats up to 55.3°C. (c) Photographs showing the de-icing capability of the printed ship.

852 nm is used to ensure sufficient light intensity for heating, Figure 9b. Only the right ship is illuminated, while the left one remains unlit. The complete experiment can be observed in Video S4 and in Figure 9e. At the beginning of the experiment, the ships are on the ice and cannot move under the magnetic field due to friction with the ice (t_0). The illuminated ship heats up, reaching 18°C (Figure 8c,d). As the ships heats up, it progressively melts the ice beneath its hull until the ice is completely drilled through (Figure 8e, 5 min). Once the ship is floating on the liquid water, it is attracted toward the magnet. The embedded chains control the boat's orientation, aligning it along the stern–bow axis, and it moves toward the region with the strongest magnetic field gradient. The ice surrounding the boat continues to melt, allowing it to move (from 5 to 17 min), with the ship carving a path through the ice.

The displacement of both ships is shown in Figure 8f. When not illuminated, the ship remains stationary on the ice, Since it produces no heat. The displacement of the illuminated ship occurs in distinct stages. Before 5 min, the ship does not move until the ice beneath it is fully melted. A noticeable step occurs between 2 and 3 min, corresponding to a reorientation of the boat as the ice melts, allowing it to align with the magnetic field. After 5 min of illumination, the displacement begins to increase once the boat reaches the water surface. Without the magnetic field and under illumination alone, the boat would stay still while the ice keeps melting beneath it. The motion of the system is governed by two physically distinct and sequential mechanisms. First, the displacement speed of the device is fundamentally limited by the ice-melting kinetics, rather than by magnetic actuation itself. The microrobot can only move once a liquid water layer is generated beneath it, and its velocity is therefore controlled by photothermal ice melting. For this reason, we developed a photothermal model, provided in the Supporting Information, to quantify the melting-driven displacement rate as a function of ice temperature and light intensity (Figure 9g; Figure S10), photothermal conversion efficiency (Figure S11), and effective floating thickness (Figure S12). This model captures the dominant parameters governing motion onset and speed during de-icing. As shown in Figure 9g, colder ice acts as a strong thermal sink, increasing both the sensible heating requirement and diffusion losses, which slows down melting and motion. In contrast, warm ice reduces both contributions, allowing faster melting and thus faster lateral displacement. Higher laser power density can compensate for thermal losses and enables efficient motion, especially at higher ice temperatures. Another experimental lever to improve motion is the floating thickness, as shown in Figure 9h. Reducing the floating thickness decreases the volume of ice that needs to be heated and melted, thereby significantly increasing the speed of motion. This effect can be achieved, for instance, by lowering the density or by optimizing the ship's design. Second, once the ice is locally melted and the device is floating on water, the trajectory, orientation, and navigation are governed by magnetic actuation. To describe this regime, we implemented a separate magnetic model (Supplementary Information). This includes magnetic simulations describing the force- and torque-driven motion of the printed object under an external magnetic field assuming that is navigating on liquid water describing the configuration in which ice is locally melted. The microrobot is modeled as a magnetic dipole operating in an overdamped regime, enabling quantitative predictions of magnetic forces, torques, trajectories, and orientation dynamics (Figure S13). Importantly, the simulated motion and alignment behavior (Figure S14 and Video S5) are in good agreement with experimental observations

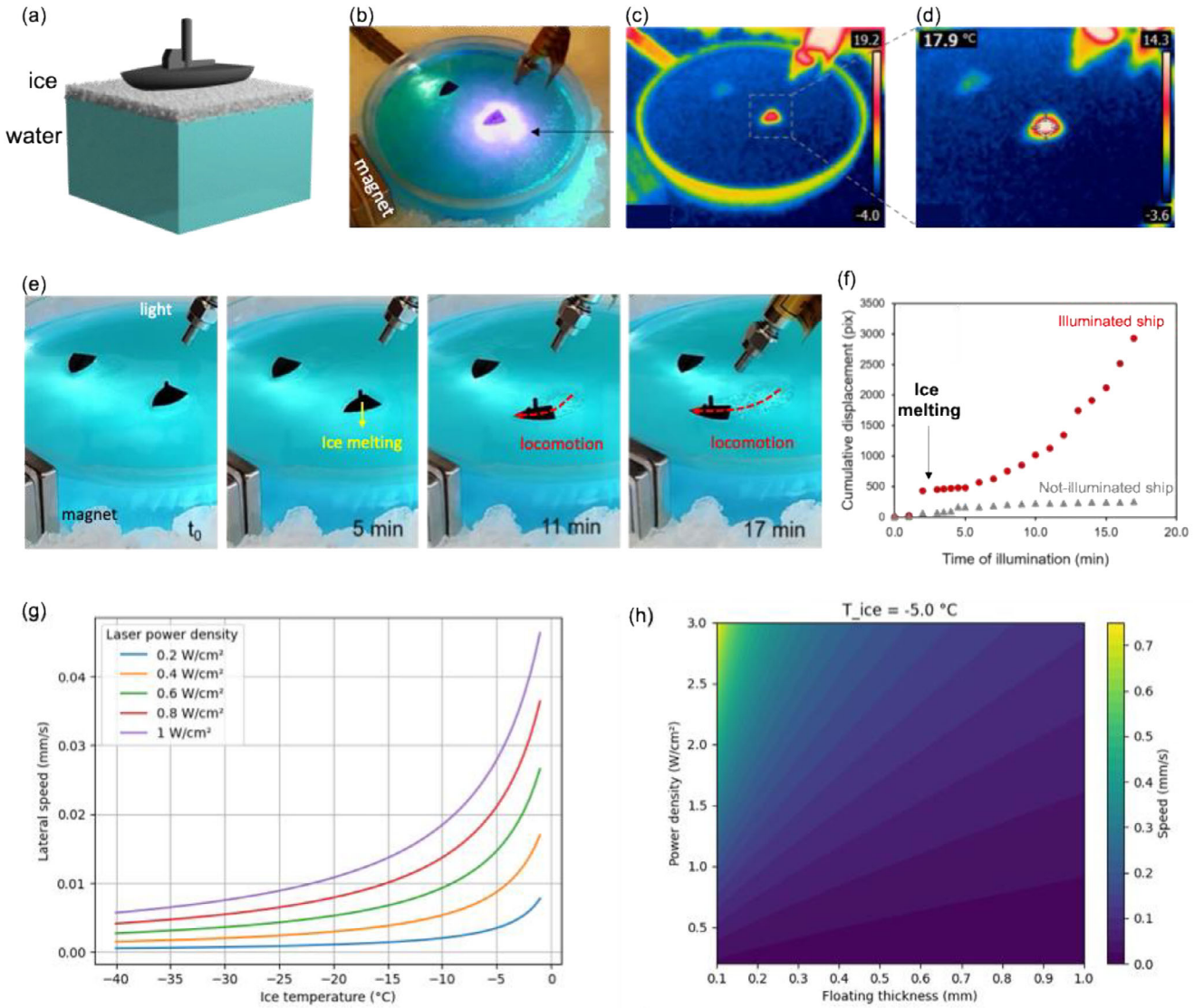

FIGURE 9 | De-icing in sea ice with magneto-plasmonic icebreaker ship. (a) Schematic of the magneto-plasmonic icebreaker ship. (b) Photograph showing that only one ship is illuminated by the light source. (c) and (d) Thermal mapping images: only the illuminated ship heats up to 18°C. (e) Time-lapse photographs of the experiment: the illuminated ship moves toward the magnet under the light, first melting the ice beneath its hull (t_0 to 5 min) and then progressively melting the surrounding ice as it continues moving (5–17 min). (f) Cumulative displacement of each ship over time: only the illuminated ship moves after piercing the ice (5 min). The step observed during the first two minutes for the right ship is due to its reorientation with the magnetic field as the ice beneath the ship melts. (g) Evolution of the lateral speed as function of the ice temperature and of the laser intensity. (h) Evolution of the ship speed as function of the power density and of the floating thickness of the ship ($T_{ice} = -5°C$).

(Figure S15 and Video S6), thereby confirming the proposed magnetic actuation mechanism.

At last, to assess environmental stability, additional photothermal and durability tests were performed under harsher conditions, including repeated thermal cycling at −20°C with controlled humidity and air flow (see Figures S16 and S17). As shown in Figure S16c, the temperature of the ship upon irradiation remains unchanged across all cycles, indicating that the photothermal heating capability is fully preserved. We investigated photothermal heating at temperatures down to −20°C (Figure S17a) and as function of the laser power (Figure S17b). These results indicate that lowering the ice temperature down to −20°C the T of the ship decreases linearly as expected. Importantly even at −20°C the temperature of the ship remains positive and allow de-icing. As shown in Figure S17b, even at −20°C, the temperature of the ship can be increased by increasing the light intensity demonstrating the potential of the approach in harsher conditions.

3 | Conclusion

In this work, we proposed a novel approach of 4D printed multifunctional device enabling spatio-temporal control of de-icing. By leveraging two stimuli, magnetic fields for spatial positioning and light for temperature activation, we were able to control both the location and speed of ice melting precisely. The integration of magneto-plasmonic fillers in a photosensitive resin, printed using magnetic-assisted DLP, enabled the formation of chain-like microstructures with anisotropic magneto-responsive

properties. By investigating the optical response by hyperspectral microscopy, we demonstrated that the photothermal efficiency can be modulated by controlling the grafting density of plasmonic particles within the self-assembled magneto-plasmonic chains. The heating intensity can be controlled by adjusting the object's design, such as its thickness, or by modifying the light's wavelength and intensity after the object has been printed. This combination of design flexibility and light control makes the material highly effective for applications like de-icing. As proof-of-concept we designed an icebreaker ship, in which de-icing is triggered by light while locomotion by magnetic field. Beyond this study, this first example of 4D printing for deicing applications represents a first step toward for the design of soft-robots working in severe environments. More broadly, this approach based on multi stimuli-responsive and multifunctional materials opens unique perspectives for the conception for more autonomous systems such as self-regulating, adaptive, reconfigurable, and time-programmable devices [29].

4 | Experimental Section/Methods

4.1 | Materials and Reagents

For the resin, bisphenol A ethoxylate diacrylate (EO/phenol = 2, Mn = 512 g/mol) was used as a monomer. Bis(2,4,6-trimethylbenzoyl) phenylphosphine oxide (BAPO) was chosen as a photoinitiator. They were both bought from Sigma–Aldrich. For magnetic nanoparticles synthesis, iron(III)acetylacetonate (>99%) was bought from ACROS Organics, triethanolamine (≥99%), diethylene glycol (>99%), poly(ethylene imine) (branched, average Mw ≈800 g.mol^{-1} by LS, average Mn ≈600 by GPC) from Sigma-Aldrich, and ethylene glycol (99.8%) from fisher scientific. For gold nanoparticles, tetrachloroauric(III) acid trihydrate (≥99.9%) and trisodium citrate dihydrate (≥99%) were bought from Sigma–Aldrich.

4.2 | Synthesis of Magnetite Functionalized With PEI

The magnetic nanoparticles are synthesized with a modified protocol described by Fiedler et al. In a typical synthesis, 90 mL diethylene glycol and 10 mL of ethylene glycol were heated up to 80°C in a 250 mL round-bottomed flask under stirring (400 rpm). After reaching the reaction temperature, 2.0 g of iron(III)acetylacetonate (iron precursor) was added in the reaction solution. The solution is stirred for 45 min. Then, 6.0 g of branched polyethyleneimine was added to the system, which was again stirred for 45 min. Finally, 6.74 g of triethanolamine were added to the reaction solution and the solution was again stirred for 45 min. The solution was then transferred into a Teflon-lined stainless-steel autoclave of 200 mL and heated up to 200°C for 12 h, with a heating ramp of 3 K min^{-1}. The obtained nanoparticles were first collected via magnetic separation. Then, they were first washed in isopropanol by using two steps of centrifugation. One centrifugation of 5 min at 1000 rpm is first realized to take away the biggest particles. The solution of the first centrifugation is transferred into new vials for a second centrifugation 15 min at 12 000 rpm. The particles are collected and washed a second time with isopropanol (15 min at 12 000 rpm), and washed two additional times with milliQ water with the same parameters. The particles are dispersed in water, transferred into a vial and collected by magnetic separation to be finally vacuum-dried over night at 25°C.

4.3 | Synthesis of Gold Nanoparticles

Gold nanoparticles are synthesized with a Turkevitch method. For the typical synthesis, 195 mL of water and 5 mL of a 100 mM solution of tetrachloroauric(III) acid trihydrate (0.5 mmol) are added in a 500 mL round-bottomed flask and heated to reflux with strong stirring (800 rpm). During heating, a solution of trisodium citrate dihydrate (TSC) at 1.06% $_{wt}$ is prepared in a vial and heated at 85°C. After at least 15 min at reflux, 52 mL of the hot TSC solution (2 mmol) is quickly added to the round-bottomed flask. After 10 min of reaction, the heater is stopped but the stirring is conserved. The solution is let to cool-down to at least to 70°C before removing the oil bath to finally reach room temperature.

4.4 | Synthesis of MNP@Au Raspberries

For MNP@Au_26, 125 mg of the previously synthesized magnetic particles are dispersed into 12.5 mL of water by sonication for 5 min. This solution is then transferred to a 500 mL vial. The totality of the previously synthesized gold nanoparticles solution is added to the 500 mL vial. The mixture is put into an ultrasonic bath for 10 min. The particles are magnetically separated (at least 1 h) and then washed in 250 mL of milliQ water for 20 min in ultrasonic bath. The particles are magnetically collected and finally dispersed for conservation at 10 mg mL^{-1} (of MNP) in ethanol. For MNP@Au_3, only half of the gold NPs solution is used for 125 mg of magnetic NPs. The gold NPs solution is diluted by 4 before being added into the 500 mL with the dispersed magnetic nanoparticles. Otherwise, the protocol is the same than for MNP@Au_26. The highest grafting is measured on three different synthesis and averaged.

4.5 | Resin Formulation

The resin is composed of bisphenol A ethoxylate diacrylate (Mn ≈512 g/mol, EO/phenol = 2) as a monomer, BAPO as photoinitiator (2% of monomer mass), and acetone (10% of monomer mass). BAPO is dissolved in acetone by gently heating up the solution to 40°C. The photoinitiator solution is then added to the monomer and the mixture is stirred with a mechanical stirrer at 500 rpm. After storing, the formulation is shacked before use for printing. For formulation loaded with MNP, the appropriate powder mass is first dispersed in ethanol at 10 mg mL^{-1} by sonication for 5 min. Then, the particles are collected by magnetic separation and the maximum of ethanol is removed from the vial. Directly on the particles, the appropriate mass of resin is added. The formulation is manually stirred and sonicated for 10 min, before use for printing. For formulation loaded with MNP@Au, the particles are already dispersed at 10 mg mL^{-1} of MNP in ethanol. The appropriate volume is taken (after short sonication of the stock solution) with a micropipette and transferred into a vial for the

formulation, and the same protocol is applied. For the calculation of the loading, the quantity of particles is calculated using the mass of MNP per hundred mass of BEDA (phB).

4.6 | Films of Resin on Glass Substrate

The films used for optical characterizations and heating measurements with light intensity were made by roll coating. On a glass substrate, a droplet of the formulation was deposited at one extremity of the substrate and manually spread on the surface using a hand coating roller to form a thin film. The final film thickness was approximately 10 µm. The resin is then polymerized by exposition to a UV light.

4.7 | Printing Parameters

The formulations were 3D-printed using a RobotFactory HD 2.0 DLP printer (nominal resolution of 50 µm in the *x*–*y* plane, maximum resolution in z-direction of 10 µm) equipped with a broadband projector emitting in the visible range (5.7 mW cm^{-2}), at the exception of the final boat for the proof of concept that was printed with an Asiga Max X27 printer (nominal resolution of 27 µm in the *x*–*y* plane, maximum resolution in z-direction of 10 µm), equipped with light at 385 nm (55 mW cm^{-2}). On RobotFactory, for 0.5 phB loading of MNP, layers of 50 µm were printed with 1.5 s per layer, and 3 s for bottom layers (3 layers). For 0.5 phB of MNP@Au_26, layers of 25 µm were printed with 0.7 s per layer, and 3 s for bottom layers (6 layers). 1 phB loading of MNP formulation was printed with layers of 30 µm with exposition of 1.6 s per layer, and 6 s for the first five layers. 1 phB loading of MNP@Au_26 formulation was printed with layers of 25 µm with exposition of 1.1 s per layer, and 7s for the first six layers. On Asiga, the 1 phB loading of MNP@Au_26 formulation was printed with layers of 50 µm with exposition of 0.5 s per layer, and 10 s for the first three layers (lifting speed set to 1 mm s^{-1}). The printer was changed to be able to use a higher light intensity favoring a better adhesion between layers.

4.8 | Characterization

4.8.1 | TEM Imaging

The TEM microscope is a Tecnai G2 Spirit Twin, equipped with a camera Orius SC 1000. Images were taken with a tension of 120 kV and a magnification of 42 000. The grids preparation consists to first prepare a solution of the particles at 40 µg mL^{-1} in milliQ water, sonicated for 3 min. One drop of the solution is then deposited on a TEM grid, which is let to dry a few hours at room conditions [56].

4.8.2 | UV–vis Spectroscopy

UV–vis measurements were done using a UV–vis spectrometer (CARY 5000, Agilent Technologies) in absorbance mode. For liquids, plastic cells were used. Measurements were also conducted on films supported on glass substrate. For those measurements, the substrate is fixed perpendicularly to the beam.

4.8.3 | Hyperspectral Microscopy

The spectral imaging was performed by a Cytoviva hyperspectral microscopy (HIS) system in transmission dark-field mode [57]. The scattered light from the particles was collected using a 100x objective. The resulting hyperspectral image was analyzed using ENVI software, extracting the scattering spectrum for each pixel and the scattering spectrum averaged on the full image [48, 49]. The spectra were normalized by the scattering value at 450 nm to enable comparison.

4.8.4 | Room Temperature Hysteresis Loops

Room temperature hysteresis loops were performed at 300K with a vibrating-sample magnetometer, with a frequency of 40 Hz and peak amplitude of 2 mm. The samples were mounted on a quartz sample-holder rod and submitted to a magnetic field (H) ranging in the interval $-25\ kOe < H < 25\ kOe$.

4.8.5 | Optical Microscope for Chains

Optical microscopy observations for alignment of MNP particles were performed with a Leica DM 2500 m equipped with a camera to follow in situ the evolution of the tested systems. The objective lenses had 50x magnification.

4.8.6 | Thermal Measurements

The laser at 852 nm was a MDL-III-852nm-1 W laser provided by Changchun New Industries Optoelectronics Tech. Co. (spot size around 10 mm^2). Photoheating measurements are done using a FLIR E4 thermal camera calibrated for the appropriate range of measured temperature. Samples are held perpendicularly to the laser beam. The camera is oriented toward the sample surface and maintained under the laser beam, to be the closest possible from a direct view of the surface of the sample. The heat ΔT calculated is the difference between the temperature of the irradiated spot on the sample surface after 5 min of illumination and the temperature before illumination (usually around 18°C–20°C). The values are averaged on 3 measurements at different locations on the sample surface.

4.8.7 | Rheological Measurements

Viscosity is measured using an Anton Paar rheometer, using parallel plates of 50 mm of diameter, with a gap of 1 mm, at 20°C. A gradient of shear is applied, from 0.01 to 10 s^{-1} with a logarithmic ramp. The given viscosity is measured at 5 Hz, where the viscosity is constant with shear rate, and averaged on 3 measurements.

Acknowledgements

This work was supported by the Commissariat a l'Energie Atomique et aux Energies Alternatives (CEA) through the project Quattro-D (PTC/MP/2022) and by the European Research Council (ERC) under

European Union's Horizon 2020 Programme (Grant Agreement no. 803220, TEMPORE). The authors thank Othmane Darouich for the support on TEM characterization and David Hrabovsky for VSM measurements. G.R. thanks Pierre Bourdon for his assistance in installing the magnetic device on the Asiga Max DLP printer.

Open access publication funding provided by COUPERIN CY26.

Conflicts of Interest

The authors declare no conflicts of interest.

Data Availability Statement

The data that support the findings of this study are available from the corresponding author upon reasonable request.

References

1. G. Prashar, H. Vasudev, and D. Bhuddhi, "Additive Manufacturing: Expanding 3D Printing Horizon in Industry 4.0," *International Journal on Interactive Design and Manufacturing* 17 (2022): 2221–2235, https://doi.org/10.1007/s12008-022-00956-4.

2. "Additive Manufacturing Market Size to Hit USD 110.13 Bn by 2033," https://www.precedenceresearch.com/additive-manufacturing-market.

3. "The Emergence of 4d Printing?," in Skyllar Tibbits (2013).

4. M. Bodaghi, L. Wang, F. Zhang, et al., "4D Printing Roadmap," *Smart Materials and Structures* 33 (2024): 113501, https://doi.org/10.1088/1361-665X/ad5c22.

5. J. Wang, Z. Wang, Z. Song, L. Ren, Q. Liu, and L. Ren, "Biomimetic Shape–Color Double-Responsive 4D Printing," *Advanced Materials Technologies* 4 (2019): 1900293.

6. Q. Ge, C. K. Dunn, H. J. Qi, and M. L. Dunn, "Active Origami by 4D Printing," *Smart Materials and Structures* 23 (2014): 094007.

7. E. Yarali, M. J. Mirzaali, A. Ghalayaniesfahani, A. Accardo, P. J. Diaz-Payno, and A. A. Zadpoor, "4D Printing for Biomedical Applications," *Advanced Materials* 36 (2024): 2402301.

8. Y. Mao, K. Yu, M. S. Isakov, J. Wu, M. L. Dunn, and H. J. Qi, "Sequential Self-Folding Structures by 3D Printed Digital Shape Memory Polymers," *Scientific Reports* 5 (2015): 13616.

9. B. Peng, Y. Yang, K. Gu, E. J. Amis, and K. A. Cavicchi, "Digital Light Processing 3D Printing of Triple Shape Memory Polymer for Sequential Shape Shifting," *ACS Materials Letters* 1 (2019): 410–417.

10. M. C. Ratri, J. Suh, J. Ryu, B. G. Chung, and K. Shin, "Formulation of Three-Dimensional, Photo-Responsive Printing Ink: Gold Nanorod-Hydrogel Nanocomposites and their Four-Dimensional Structures That Respond Quickly to Stimuli," *Journal of Applied Polymer Science* 140 (2023): 53799.

11. Y. Wang, E. Sachyani Keneth, A. Kamyshny, G. Scalet, F. Auricchio, and S. Magdassi, "4D Multimaterial Printing of Programmable and Selective Light-Activated Shape-Memory Structures With Embedded Gold Nanoparticles," *Advanced Materials Technologies* 7 (2022): 2101058.

12. Y. Kim, H. Yuk, R. Zhao, S. A. Chester, and X. Zhao, "Printing Ferromagnetic Domains for Untethered Fast-Transforming Soft Materials," *Nature* 558 (2018): 274–279.

13. C. Ma, S. Wu, Q. Ze, et al., "Magnetic Multimaterial Printing for Multimodal Shape Transformation With Tunable Properties and Shiftable Mechanical Behaviors," *ACS Applied Materials & Interfaces* 13 (2021): 12639–12648.

14. A. Cortés, A. Cosola, M. Sangermano, et al., "DLP 4D-Printing of Remotely, Modularly, and Selectively Controllable Shape Memory Polymer Nanocomposites Embedding Carbon Nanotubes," *Advanced Functional Materials* 31 (2021): 2106774.

15. A. Sydney Gladman, E. A. Matsumoto, R. G. Nuzzo, L. Mahadevan, and J. A. Lewis, "Biomimetic 4D Printing," *Nature Materials* 15 (2016): 413–418.

16. J. Wu, Z. Zhao, X. Kuang, C. M. Hamel, D. Fang, and H. J. Qi, "Reversible Shape Change Structures by Grayscale Pattern 4D Printing," *Multifunctional Materials* 1 (2018): 015002.

17. Y. Hu, Z. Wang, D. Jin, et al., "Botanical-Inspired 4D Printing of Hydrogel at the Microscale," *Advanced Functional Materials* 30 (2020): 1907377.

18. L. Chen, Y. Zhang, H. Ye, et al., "Color-Changeable Four-Dimensional Printing Enabled With Ultraviolet-Curable and Thermochromic Shape Memory Polymers," *ACS Applied Materials & Interfaces* 13 (2021): 18120–18127.

19. U. Bozuyuk, O. Yasa, I. C. Yasa, H. Ceylan, S. Kizilel, and M. Sitti, "Light-Triggered Drug Release From 3D-Printed Magnetic Chitosan Microswimmers," *ACS Nano* 12 (2018): 9617–9625.

20. S. Lantean, G. Barrera, C. F. Pirri, et al., "3D Printing of Magnetoresponsive Polymeric Materials with Tunable Mechanical and Magnetic Properties by Digital Light Processing," *Advanced Materials Technologies* 4 (2019): 1900505.

21. X. Lan, L. Liu, C. Pan, et al., "Smart Solar Array Consisting of Shape-Memory Releasing Mechanisms and Deployable Hinges," *AIAA Journal* 59 (2021): 2200–2213.

22. Q. Ge, A. H. Sakhaei, H. Lee, C. K. Dunn, N. X. Fang, and M. L. Dunn, "Multimaterial 4D Printing With Tailorable Shape Memory Polymers," *Scientific Reports* 6 (2016): 31110.

23. A. K. Mishra, T. J. Wallin, W. Pan, et al., "Autonomic Perspiration in 3D-Printed Hydrogel Actuators," *Science Robotics* 5 (2020): aaz3918.

24. M. A. Mackey, M. R. K. Ali, L. A. Austin, R. D. Near, and M. A. El-Sayed, "The Most Effective Gold Nanorod Size for Plasmonic Photothermal Therapy: Theory and In Vitro Experiments," *The Journal of Physical Chemistry B* 118 (2014): 1319–1326.

25. B. Ciraulo, J. Garcia-Guirado, I. de Miguel, J. Ortega Arroyo, and R. Quidant, "Long-Range Optofluidic Control With Plasmon Heating," *Nature Communications* 12 (2021): 2001.

26. F. Thorimbert, M. C. Rivadeneira, and M. Faustini, "Self-Assembling Cracks to Fabricate Antireflective Antifogging Metasurfaces," *Advanced Optical Materials* 13 (2025): 2500079.

27. P. Wang, "Emerging Investigator Series: The Rise of Nano-Enabled Photothermal Materials for Water Evaporation and Clean Water Production by Sunlight," *Environmental Science: Nano* 5 (2018): 1078–1089.

28. C. Byun, D. R. Ceratti, C. Mimoso, C. Boissière, and M. Faustini, "A Homeostatic Photonic Device Integrating Vapor-Regulated Thermo-Optical Feedback Mechanisms," *Advanced Functional Materials* 35 (2025): 2424453.

29. H. Amyar, D. R. Ceratti, H. Benisty, A. Cattoni, M. Besbes, and M. Faustini, "Self-Regulating and Self-Oscillating Metal-Organic Framework Hybrid Plasmonic Metasurfaces," *Nature Communications* 16 (2025): 10392.

30. F. Thorimbert, M. Odziomek, D. Chateau, S. Parola, and M. Faustini, "Programming Crack Patterns With Light in Colloidal Plasmonic Films," *Nature Communications* 15 (2024): 1156.

31. Y. Wu, L. Dong, X. Shu, Y. Yang, P. Feng, and Q. Ran, "Recent Advancements in Photothermal Anti-Icing/Deicing Materials," *Chemical Engineering Journal* 469 (2023): 143924.

32. M. Mao, J. Wei, B. Li, L. Li, X. Huang, and J. Zhang, "Scalable Robust Photothermal Superhydrophobic Coatings for Efficient Anti-Icing and De-Icing in Simulated/Real Environments," *Nature Communications* 15 (2024): 9610.

33. J. Pyeon, S. M. Park, J. Kim, et al., "Plasmonic Metasurfaces of Cellulose Nanocrystal Matrices With Quadrants of Aligned Gold Nanorods for Photothermal Anti-Icing," *Nature Communications* 14 (2023): 8096.

34. S. Lantean, I. Roppolo, M. Sangermano, et al., "Magnetoresponsive Devices With Programmable Behavior Using a Customized Commercial Stereolithographic 3D Printer," *Advanced Materials Technologies* 7 (2022): 2200288.

35. E. Aïdonidis, A. Cosola, P. Bourdon, et al., "Encoding Magnetic Anisotropies in Digital Light Processing 3D Printing," *Advanced Functional Materials* (2025): e23995, https://doi.org/10.1002/adfm.202523995.

36. K. Halbach, "Design of Permanent Multipole Magnets With Oriented Rare Earth Cobalt Material," *Nuclear Instruments and Methods* 169 (1980): 1–10.

37. W. Shen, C. Wang, X. Yang, et al., "Synthesis of Raspberry-Like Nanogapped Fe_3O_4@Au Nanocomposites for SERS-Based Lateral Flow Detection of Multiple Tumor Biomarkers," *Journal of Materials Chemistry C* 8 (2020): 12854–12864.

38. J. Kimling, M. Maier, B. Okenve, V. Kotaidis, H. Ballot, and A. Plech, "Turkevich Method for Gold Nanoparticle Synthesis Revisited," *The Journal of Physical Chemistry B* 110 (2006): 15700–15707.

39. R. Fiedler, B. Beizinger, P. Walther, and M. Lindén, "Synthesis of Highly Monodisperse Superparamagnetic Iron Oxide Core@Mesoporous Silica Shell Particles With Independently Tunable Size, and Porosity," *Microporous and Mesoporous Materials* 340 (2022): 112027.

40. A. Cosola, I. Roppolo, F. Frascella, et al., "4D Printing of Multifunctional Devices Induced by Synergistic Role of Magnetite and Silver Nanoparticles in Polymeric Nanocomposites," *Advanced Functional Materials* 34 (2024): 2406226.

41. S. Lantean, I. Roppolo, M. Sangermano, M. Hayoun, H. Dammak, and G. Rizza, "Programming the Microstructure of Magnetic Nanocomposites in DLP 3D Printing," *Additive Manufacturing* 47 (2021): 102343.

42. V. Neu, C. Schulze, M. Faustini, et al., "Probing the Energy Barriers and Magnetization Reversal Processes of Nanoperforated Membrane Based Percolated Media," *Nanotechnology* 24 (2013): 145702, https://doi.org/10.1088/0957-4484/24/14/145702.

43. M. Grobis, C. Schulze, M. Faustini, et al., "Recording Study of Percolated Perpendicular Media," *Applied Physics Letters* 98 (2011): 192504, https://doi.org/10.1063/1.3587635.

44. E. Vargas, J. C. Denardin, R. Lavín, P. Mascaró, C. Chaneac, and T. Coradin, "Magnetization Analysis of Oriented Chains of Hexagonal Cobalt Nanoplates," *Journal of Applied Physics* 115 (2014): 17B521.

45. Z. Chehadi, C. Boissière, C. Chanéac, and M. Faustini, "Nanoconfined Water Vapour as a Probe to Evaluate Plasmonic Heating," *Nanoscale* 12 (2020): 13368–13376.

46. Y. Wy, H. Jung, J. W. Hong, and S. W. Han, "Exploiting Plasmonic Hot Spots in Au-Based Nanostructures for Sensing and Photocatalysis," *Accounts of Chemical Research* 55 (2022): 831–843.

47. S. H. C. Askes and E. C. Garnett, "Ultrafast Thermal Imprinting of Plasmonic Hotspots," *Advanced Materials* 33 (2021): 2105192.

48. M. L. De Marco, O. Smith, F. Thorimbert, et al., "Self-Regulating VO_2 Photonic Pigments," *Chemistry of Materials* 35 (2023): 7164–7174.

49. C. Avci, M. L. De Marco, C. Byun, et al., "Metal–Organic Framework Photonic Balls: Single Object Analysis for Local Thermal Probing," *Advanced Materials* 33 (2021): 2104450.

50. L. Mikoliunaite, M. Talaikis, A. Michalowska, et al., "Thermally Stable Magneto-Plasmonic Nanoparticles for SERS With Tunable Plasmon Resonance," *Nanomaterials* 12 (2022): 2860.

51. J. H. Yoon, F. Selbach, L. Schumacher, J. Jose, and S. Schlücker, "Surface Plasmon Coupling in Dimers of Gold Nanoparticles: Experiment and Theory for Ideal (Spherical) and Nonideal (Faceted) Building Blocks," *ACS Photonics* 6 (2019): 642–648.

52. Y. Wang, Z. Gao, Z. Han, et al., "Aggregation Affects Optical Properties and Photothermal Heating of Gold Nanospheres," *Scientific Reports* 11 (2021): 898.

53. C. Brissaud, W. Chaâbani, J. Giráldez-Martínez, et al., "Faceted 3D Supercrystals for Plasmonic Photocatalysis: Design, Reactivity, and Operando Studies," *Small Structures* 6 (2025): 202500481.

54. S. K. Ghosh and T. Pal, "Interparticle Coupling Effect on the Surface Plasmon Resonance of Gold Nanoparticles: From Theory to Applications," *Chemical Reviews* 107 (2007): 4797–4862.

55. D. K. Roper, W. Ahn, and M. Hoepfner, "Microscale Heat Transfer Transduced by Surface Plasmon Resonant Gold Nanoparticles," *The Journal of Physical Chemistry C* 111 (2007): 3636–3641.

56. M. Gayrard, J. Voronkoff, C. Boissière, et al., "Replacing Metals With Oxides in Metal-Assisted Chemical Etching Enables Direct Fabrication of Silicon Nanowires by Solution Processing," *Nano Letters* 21 (2021): 2310–2317.

57. H. Amyar, C. Byun, M. Besbes, et al., "In Situ Infrared Spectroscopic Ellipsometry as a Tool to Probe the Formation of Sol–Gel Based Mesoporous Films," *Journal of Sol-Gel Science and Technology* 116 (2023): 706–717.

Supporting Information

Additional supporting information can be found online in the Supporting Information section.

Supporting File 1: adfm74754-sup-0001-SuppMat.docx.
Supporting File 2: adfm74754-sup-0002-VideoS1.mp4.
Supporting File 3: adfm74754-sup-0003-VideoS2.mp4.
Supporting File 4: adfm74754-sup-0004-VideoS3.mp4.
Supporting File 5: adfm74754-sup-0005-VideoS4.mp4.
Supporting File 6: adfm74754-sup-0006-VideoS5.mp4.
Supporting File 7: adfm74754-sup-0007-VideoS6.mp4.